Chemical
Science

ROYAL SOCIETY
OF CHEMISTRY

EDGE ARTICLE

View Article Online
View Journal | View Issue

Cite this: *Chem. Sci.*, 2024, **15**, 16637

All publication charges for this article have been paid for by the Royal Society of Chemistry

Received 23rd July 2024
Accepted 15th September 2024

DOI: 10.1039/d4sc04884a

rsc.li/chemical-science

Size disproportionation among nanocluster transformations†

Chen Zhu,‡ Luyao Lu,‡ Fei Li, Xi Kang * and Manzhou Zhu

Controllable transformation is a prerequisite to the in-depth understanding of structure evolution mechanisms and structure–property correlations at the atomic level. Most transformation cases direct the directional evolution of nanocluster sizes, *i.e.*, size-maintained, size-increased, or size-reduced transformation, while size disproportionation was rarely reported. Here, we report the Au-doping-induced size disproportionation of nanocluster transformation. Slight Au-doping on the bimetallic $(AgCu)_{43}$ nanocluster produced its trimetallic derivative, $(AuAgCu)_{43}$, following a size-maintained transformation. By comparison, the $(AgCu)_{43}$ nanocluster underwent a size-disproportionation transformation under heavy Au alloying, leading to the formation of size-reduced $(AuAgCu)_{33}$ and size-increased $(AuAgCu)_{56}$ nanoclusters simultaneously. Such a size disproportionation among the nanocluster transformations was verified by the thin-layer chromatography analysis. This work presented a novel nanocluster transformation case with a size disproportionation characteristic, expected to provide guidance for the understanding of cluster size evolutions.

1 Introduction

Metal nanoclusters, bridging organometallic complexes and plasmonic nanoparticles, have emerged as a captivating subject of study owing to their atomically precise structures, discrete electronic energy levels, and strong quantum size effect.[1–6] The physicochemical properties of metal nanoclusters display a notable sensitivity to their structures, rendering them ideal platforms for investigating atomic-defined correlations between structures and properties.[7–18] Besides, various potential applications based on such ultrasmall nanomaterials have been found in catalysis, optoelectronics, phototherapy, chemical sensing, and so on.[19–25] The controllable preparation of metal nanoclusters is a prerequisite to their follow-up research and downstream applications.[1–3] To date, several efficient approaches have been proposed to trigger nanocluster transformations and dictate nanocluster structures, mainly including heteroatom doping, ligand exchanging, counterion substituting, intercluster assembling, and environmental regulation.[26–35]

Based on nanocluster transformations from precision to precision, several mechanisms of structural evolutions have been mapped out at the atomic level.[26–30] Because of the thermodynamic and kinetic factors, most transformation cases direct the directional evolution of nanocluster sizes, *i.e.*, size-maintained, size-increased, or size-reduced transformation,[31–46] while size disproportionation was rarely reported, probably due to that separation and crystallization of poly-dispersed cluster products were difficult. Disproportionation usually refers to a reaction in which oxidation and reduction processes happen simultaneously, leading to one part of the molecule being oxidized while another part being reduced.[47] To date, the concept of disproportionation has been extended to the field of nanomaterial study, where one nanomolecular precursor could convert to two or more different nanomolecular products with individually increasing and decreasing sizes.[48,49] It is important and necessary to construct an atomically precise platform for exploring size disproportionation among nanocluster transformations, which hopefully allows for an in-depth understanding of nanocluster size evolutions.

Herein, we report the size disproportionation of the nanocluster transformation induced by the Au-alloying process (Scheme 1). The slight Au doping to the $Ag_{26}Cu_{17}(SR)_{30}(PPh_3)_7$ nanocluster ($(AgCu)_{43}$ for short SR = 4-(trifluoromethylthio)phenol) with a core@shell configuration gave rise to a structure-maintained trimetallic $Au_2Ag_{24}Cu_{17}(SR)_{30}(PPh_3)_7$ nanocluster ($(AuAgCu)_{43}$ for short), which was cocrystallized together with $Cl_1Ag_8Cu_6(SR)_{12}(PPh_3)_6$ in the crystal lattice. Furthermore, the $Au_2Ag_{24}Cu_{17}(SR)_{30}(PPh_3)_7$ nanocluster underwent size

---

Department of Chemistry and Centre for Atomic Engineering of Advanced Materials, Key Laboratory of Structure and Functional Regulation of Hybrid Materials of Ministry of Education, Anhui Province Key Laboratory of Chemistry for Inorganic/Organic Hybrid Functionalized Materials, Anhui University, Hefei, Anhui 230601, P. R. China. E-mail: kangxi_chem@ahu.edu.cn

† Electronic supplementary information (ESI) available: Fig. S1–S15 and Tables S1–S4. CCDC 2370220–2370223. For ESI and crystallographic data in CIF or other electronic format see DOI: https://doi.org/10.1039/d4sc04884a

‡ C. Z. and L. L. contributed equally to this work.

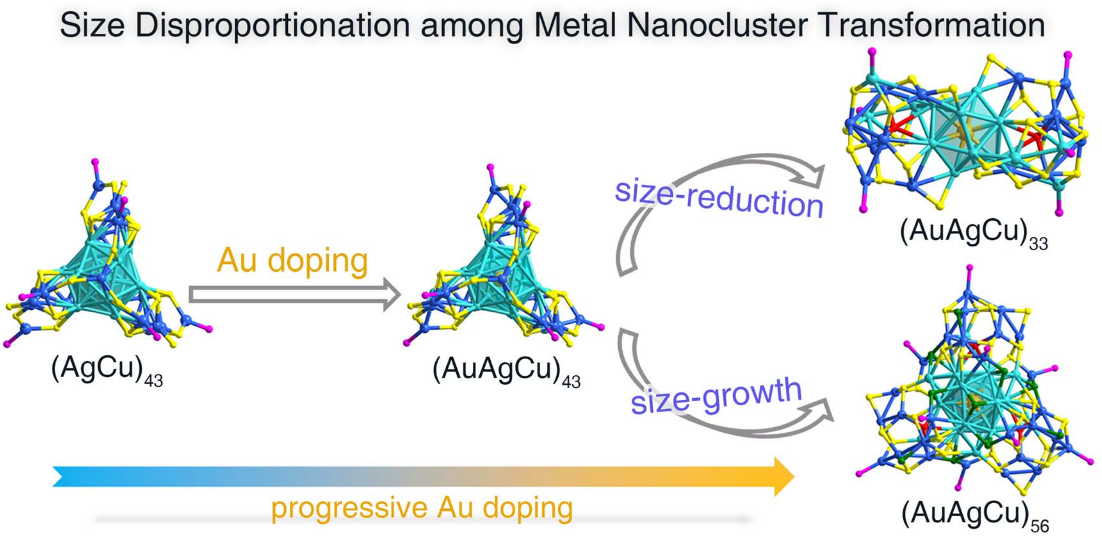

Scheme 1 Illustration of size disproportionation among the nanocluster transformations. Progressive Au doping induced successive nanocluster transformation from the $(AgCu)_{43}$ precursor into the size-maintained $(AuAgCu)_{43}$ nanocluster and then into size-disproportionated $(AuAgCu)_{56}$ and $(AuAgCu)_{33}$ nanoclusters.

disproportionation under heavy Au doping, producing size-increased $Au_2Ag_{27}Cu_{27}S_3(SR)_{30}(PPh_3)_9Cl_{11}$ ($(AuAgCu)_{56}$ for short) and size-reduced $Au_1Ag_{18}Cu_{14}S_2(SR)_{14}(PPh_3)_6$ ($(AuAgCu)_{33}$ for short). The atomically precise structures of such nanoclusters were determined by single-crystal X-ray diffraction (SC-XRD). Furthermore, the thin-layer chromatography (TCL) tests suggested that the $(AuAgCu)_{56}$ and $(AuAgCu)_{33}$ nanoclusters were generated simultaneously from the $(AuAgCu)_{43}$ precursor induced by the Au alloying, further demonstrating size disproportionation. This work not only described the heteroatom doping of the $(AgCu)_{43}$ nanocluster in detail but also revealed the size disproportionation phenomenon in nanoclusters.

2 Experimental methods

2.1 Materials

All following reagents were purchased from Sigma-Aldrich and used without further purification, including cupric acetylacetonate ($Cu(C_5H_7O_2)_2$, 98% metal basis), silver nitrate ($AgNO_3$, 99% metal basis), chloro(triphenylphosphine)gold(I) ($Au(PPh_3)Cl$, 98%), 4-trifluoromethyl phenylthiophenol ($C_7H_5F_3S$, 98%), triphenylphosphine ($C_{18}H_{15}P$, 99%), sodium borohydride ($NaBH_4$, 99%), methanol (HPLC grade), dichloromethane (HPLC grade), hexane (HPLC grade), and toluene (HPLC grade).

2.2 Preparation of the $(AgCu)_{43}$ nanocluster

30 mg of $AgNO_3$ was dissolved in a mixed solution of 5 mL of MeOH and 20 mL of CH_2Cl_2, and 70 mg of $Cu(C_5H_7O_2)_2$ was added to this solution. After 20 minutes, 50 mg of PPh_3 and 50 μL of 4-trifluoromethyl phenylthiophenol were added. Then, 5 mL of the aqueous solution of $NaBH_4$ (8 mg mL^{-1}) was added. The reaction was proceeded for 12 hours. The obtained solution was centrifuged at 10 000 rpm for 3 minutes, and the supernatant was collected and evaporated to get the crude product. The crude product was washed three times with hexane and methanol to get the $(AgCu)_{43}$ nanocluster.

2.3 Preparation of the $(AuAgCu)_{43}\cdot(AgCu)_{14}$ nanocluster

The as-prepared $(AgCu)_{43}$ nanocluster (10 mg) was dissolved in 50 mL of toluene. The solution was vigorously stirred with a magnetic stir bar for 10 minutes. Then, 150 μL of $Au(PPh_3)Cl$ solution (dissolved in toluene, 5 mg mL^{-1}) was added. The reaction was allowed to proceed for two hours. After that, the organic phase was rotavaporated under vacuum, and the precipitate was redissolved in CH_2Cl_2, producing the $(AuAgCu)_{43}\cdot(AgCu)_{14}$ nanocluster as determined by SC-XRD.

2.4 Preparation of $(AuAgCu)_{33}$ and $(AuAgCu)_{56}$ nanoclusters

The as-prepared $(AgCu)_{43}$ nanocluster (10 mg) was dissolved in 50 mL of toluene. The solution was vigorously stirred with a magnetic stir bar for 10 min. Then, 800 μL of $Au(PPh_3)Cl$ solution (dissolved in toluene, 5 mg mL^{-1}) was added. The reaction was allowed to proceed for two hours. After that, the organic phase was rotavaporated under vacuum, and the precipitate was redissolved in CH_2Cl_2. Then, thin-layer chromatography was used to separate and obtain $(AuAgCu)_{33}$ and $(AuAgCu)_{56}$ nanoclusters.

2.5 Crystallization of $(AgCu)_{43}$, $(AuAgCu)_{43}\cdot(AgCu)_{14}$, $(AuAgCu)_{33}$ and $(AuAgCu)_{56}$ nanoclusters

Single crystals of $(AgCu)_{43}$, $(AuAgCu)_{43}\cdot(AgCu)_{14}$, $(AuAgCu)_{33}$, and $(AuAgCu)_{56}$ nanoclusters were cultivated at room temperature by diffusing *n*-hexane into the CH_2Cl_2 solution of each nanocluster. After a week, crystals were collected, and the structures of these nanoclusters were determined.

2.6 Characterization

The optical absorption spectra of nanoclusters were recorded using an Agilent 8453 diode array spectrometer.

Electrospray ionization mass spectrometry (ESI-MS) measurements were performed using a Waters XEVO G2-XS QTof mass spectrometer. The sample was directly infused into the chamber at 5 μL min^{-1}. For preparing the ESI samples, nanoclusters were dissolved in CH_2Cl_2 (1 mg mL^{-1}) and diluted (v/v = 1 : 1) using CH_3OH.

X-ray photoelectron spectroscopy (XPS) was performed on a Thermo ESCALAB 250 equipped with a monochromated Al Kα (1486.8 eV) 150 W X-ray source, a 0.5 mm circular spot size, a flood gun to counter charging effects, and the analysis chamber base pressure lower than 1×10^{-9} mbar. The data were collected with FAT = 20 eV.

2.7 X-ray crystallography

The data collection for single-crystal X-ray diffraction (SC-XRD) of all nanocluster crystal samples was carried out on a Stoe Stadivari diffractometer under nitrogen flow, using graphite-monochromatized Cu Kα radiation (λ = 1.54186 Å). Data reductions and absorption corrections were performed using the SAINT and SADABS programs, respectively. The structure was solved by direct methods and refined with full-matrix least squares on F^2 using the SHELXTL software package. All non-hydrogen atoms were refined anisotropically, and all the hydrogen atoms were set in geometrically calculated positions and refined isotropically using a riding model. All crystal structures were treated with PLATON SQUEEZE. The diffuse electron densities from these residual solvent molecules were removed.

3 Results and discussion

The $(AgCu)_{43}$ nanocluster was prepared with a one-pot synthetic procedure by directly reducing the Ag–Cu-SR-PPh_3 complexes with $NaBH_4$ (see the ESI† for more details). $Au(PPh_3)Cl$ with a concentration of 5 mg mL^{-1} was controllably added to the toluene solution of the $(AgCu)_{43}$ nanocluster to trigger nanocluster transformation. The slight introduction of $Au(PPh_3)Cl$ (150 μL) gave rise to a size-maintained $(AuAgCu)_{43}$ nanocluster. By comparison, heavy Au doping (800 μL) resulted in the size disproportionation of the nanocluster framework, and a size-increased $(AuAgCu)_{56}$ nanocluster and a size-reduced $(AuAgCu)_{33}$ nanocluster were obtained. Single crystals of these nanoclusters were cultivated at room temperature by diffusing *n*-hexane into the CH_2Cl_2 solution of each nanocluster, and their crystal structures were determined by SC-XRD. The X-ray photoelectron spectroscopy (XPS) results of these nanoclusters were collected to further verify the successful introduction of Au heteroatoms into the cluster framework (Fig. S1 and S2†).

The chemical formulae of $(AgCu)_{43}$, $(AuAgCu)_{43}$, and $(AuAgCu)_{33}$ nanoclusters were characterized by electrospray ionization mass spectrometry (ESI-MS; Figs. S1–S5†). However, the mass signal of the $(AuAgCu)_{56}$ nanocluster was not detected in the positive or negative ion mode of ESI-MS, probably because of its difficulty in ionizing. Indeed, several PPh_3 ligands were detached from the surface of $(AgCu)_{43}$, $(AuAgCu)_{43}$, and $(AuAgCu)_{33}$ nanoclusters to assist their ionization, and thus mass signals of "cluster–$x$$PPh_3$" molecules were detected.[50–52] Besides, the ESI-MS results also demonstrated that several positions in the frameworks of $(AgCu)_{43}$, $(AuAgCu)_{43}$, and $(AuAgCu)_{33}$ alloy nanoclusters were co-occupied by different metals. For example, the mass peaks of the bimetallic $(AgCu)_{43}$ nanocluster were assigned to chemical formulae of "Ag_x-$Cu_{43-x}(SR)_{30}(PPh_3)_6$" where x ranged from 14 to 38 (Fig. S3†), illustrating that a large number of metal positions were co-occupied by Ag and Cu.[53] Such a phenomenon also existed in analyzing the ESI-MS results of trimetallic $(AuAgCu)_{43}$ and $(AuAgCu)_{33}$ nanoclusters (Fig. S4 and S5†). Of note, in the single-crystal analysis process, each position was confined as the metal with the highest proportion for a better understanding of the nanocluster structures.

Structurally, the overall structure of the $(AgCu)_{43}$ nanocluster contained a coplanar Ag_{23} kernel that was composed of two Ag_{13} icosahedral cores sharing a triangular Ag_3 surface (Fig. 1A). Such a biicosahedral Ag_{23} kernel was stabilized by three Cu_5-$Ag_1(SR)_8(PPh_3)_2$ motif structures *via* Cu–S or Cu–Ag interactions, producing an $Ag_{26}Cu_{15}(SR)_{24}(PPh_3)_6$ structure (Fig. 1B and C). Two Cu-based terminals, $Cu_1(SR)_3$ and $Cu_1(SR)_3(PPh_3)_1$, were anchored onto both ends of the above-mentioned structure (Fig. 1D–F), forming the complete $Ag_{26}Cu_{17}(SR)_{30}(PPh_3)_7$ framework (Fig. 1G). The overall configuration of $(AgCu)_{43}$ was similar to those of $Au_2Ag_{42}(SAdm)_{27}$ and $Au_1Ag_{21}(dppf)_3$(-SAdm)$_{12}$ nanoclusters from the top view (Fig. 1H and I).[54,55]

The size-maintained transformation from the bimetallic $(AgCu)_{43}$ nanocluster into its trimetallic derivative, $(AuAgCu)_{43}$, was triggered by slight Au-alloying, *i.e.*, introducing 0.75 mg of $Au(PPh_3)Cl$ to the solution containing 10 mg of the cluster. Of note, a $Cl_1Ag_8Cu_6(SR)_{12}(PPh_3)_6$ ($(AgCu)_{14}$ for short) nanocluster was also obtained with this Au-alloying process, contributing a cocrystallized system together with the $(AuAgCu)_{43}$ nanocluster (see below). Actually, we have also tried to add 0.25 or 0.5 mg of $Au(PPh_3)Cl$ to the same cluster solution, which also yielded the $(AuAgCu)_{43}\cdot(AgCu)_{14}$ cocrystallized system, while the yield was decreased relative to the 0.75 mg $Au(PPh_3)Cl$ addition. The $(AuAgCu)_{43}$ nanocluster followed the same configuration as that of the $(AgCu)_{43}$ precursor, while the innermost two Ag cores of the biicosahedral Ag_{23} kernel in $(AgCu)_{43}$ were substituted by the introduced Au heteroatoms along with the Au doping (Fig. 2A–C). The corresponding bond lengths between $(AgCu)_{43}$ and $(AuAgCu)_{43}$ nanoclusters were compared (Fig. S6†). Although the average bond length of M(icosahedral kernel)–Ag(icosahedral surface) was the same between two 43-metal-atom nanoclusters, the bond lengths in $(AuAgCu)_{43}$ nanoclusters were more uniform (Fig. S6A†). Besides, most bond lengths of Ag(icosahedral surface)–Ag(icosahedral surface) in $(AgCu)_{43}$ were much larger than those in $(AuAgCu)_{43}$. By comparison, several corresponding peripheral M–S bonds (M = Ag/Cu) were extended along with the Au doping (Fig. S6B–D†). In this context, the $(AuAgCu)_{43}$ nanocluster possessed a tighter internal connection than $(AgCu)_{43}$, yet exhibited a looser surface connection, potentially attributed

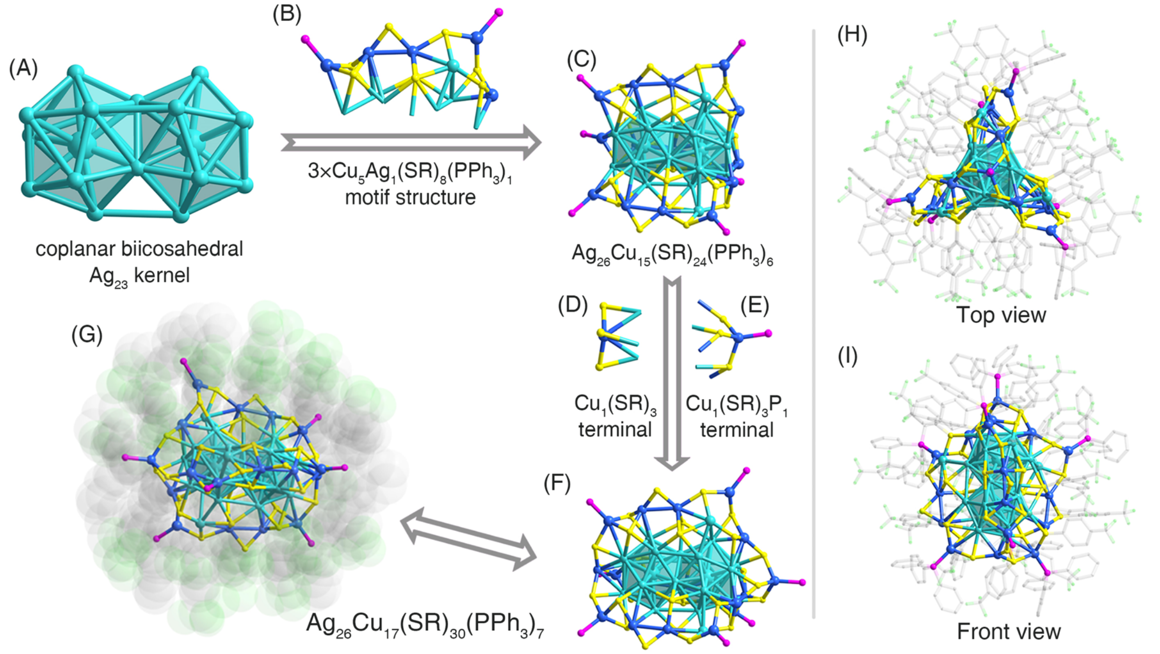

Fig. 1 Structure analysis of a $Ag_{26}Cu_{17}(SR)_{30}(PPh_3)_7$ nanocluster. (A) The coplanar biicosahedral Ag_{23} kernel. (B) Three $Cu_5Ag_1(SR)_8(PPh_3)_2$ motif structures. (C) The $Ag_{26}Cu_{15}(SR)_{24}(PPh_3)_6$ structure. (D and E) $Cu_1(SR)_3$ and $Cu_1(SR)_3(PPh_3)_1$ terminal units. (F and G) Overall structure of the $Ag_{26}Cu_{17}(SR)_{30}(PPh_3)_7$ nanocluster. (H and I) Top view and front view of the $Ag_{26}Cu_{17}(SR)_{30}(PPh_3)_7$ nanocluster. Color labels: light blue, Ag; blue, Cu; yellow, S; magenta, P; grey, C; green, Cl. For clarity, all H atoms are omitted.

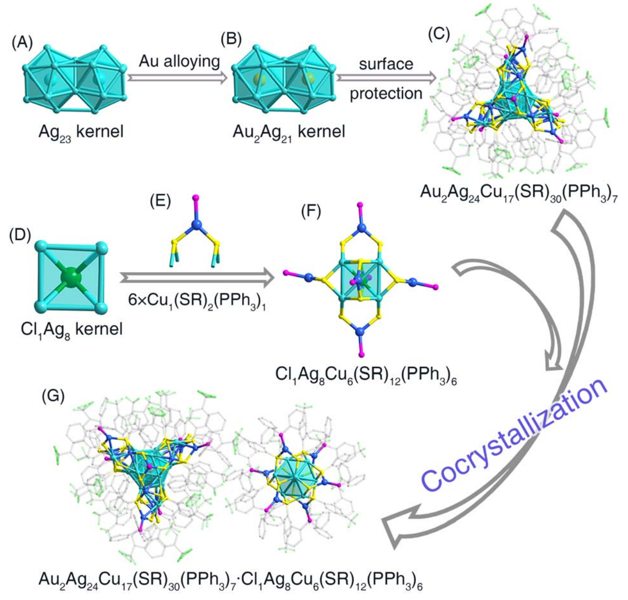

Fig. 2 Structure analysis of the $Au_2Ag_{24}Cu_{17}(SR)_{30}(PPh_3)_7{\cdot}Cl_1Ag_8Cu_6(SR)_{12}(PPh_3)_6$ cocrystallized nanocluster. (A and B) Au doping-induced alloying from the Ag_{23} kernel to the Au_2Ag_{21} kernel. (C) Overall structure of the $Au_2Ag_{24}Cu_{17}(SR)_{30}(PPh_3)_7$ nanocluster. (D) Hexahedral Cl_1Ag_8 kernel. (E) Six $Cu_1(SR)_2(PPh_3)_1$ surface motif structures. (F) Overall structure of the $Cl_1Ag_8Cu_6(SR)_{12}(PPh_3)_6$ nanocluster. (G) Cocrystallized $Au_2Ag_{24}Cu_{17}(SR)_{30}(PPh_3)_7$ and $Cl_1Ag_8Cu_6(SR)_{12}(PPh_3)_6$ nanoclusters. Color labels: light blue, Ag; blue, Cu; yellow, S; magenta, P; grey, C; green, Cl. For clarity, all H atoms are omitted.

to the incorporation of gold heteroatoms with the biicosahedral kernel.

The $(AgCu)_{14}$ cluster molecules were observed in the crystal lattice of $(AuAgCu)_{43}$ with a mole ratio of 1/2 of $(AgCu)_{14}/(AuAgCu)_{43}$. The $(AgCu)_{14}$ nanocluster should be generated along with the Au alloying and could be attributed to the decomposition of some $(AgCu)_{43}$ nanoclusters. The structure of the $(AgCu)_{14}$ nanocluster could be divided into two components: the cubic Cl_1Ag_8 kernel and six $Cu_1(SR)_2(PPh_3)_1$ surface structures (Fig. 2D and E). Each face of the Ag_8 cube was capped with a $Cu_1(SR)_2(PPh_3)_1$ unit (Fig. 2F). From the perspective of the crystalline assembly, the cocrystallization system of $(AuAgCu)_{43}$ and $(AgCu)_{14}$ nanoclusters displayed an "AA′B–AA′B" packing pattern along the *c*-axis (Fig. 2G and S7†). Abundant intramolecular and intermolecular interactions were observed among nanoclusters in the crystal lattice. Specifically, for 18 nanocluster molecules (six $(AgCu)_{14}$ and twelve $(AuAgCu)_{43}$) in a unit cell, each $(AgCu)_{14}$ nanocluster was enveloped by five $(AuAgCu)_{43}$ nanocluster molecules, while each $(AuAgCu)_{43}$ nanocluster was surrounded by four $(AgCu)_{14}$ and four $(AuAgCu)_{43}$ nanocluster molecules (Fig. S8†). Abundant intramolecular $\pi\cdots\pi$, C–H$\cdots\pi$, and C–H$\cdots$F interactions were also observed in $(AuAgCu)_{43}$ and $(AgCu)_{14}$ nanoclusters at the molecular level (Fig. S8†). Furthermore, several intermolecular C–H$\cdots\pi$ and C–H$\cdots$F interactions were detected between adjacent $(AgCu)_{14}$ and $(AuAgCu)_{43}$ nanoclusters, with an average distance of 2.889 Å for C–H$\cdots\pi$ and 2.765 Å for C–H$\cdots$F (Fig. S10†). These weak forces collectively contributed to the formation of the cocrystallized system.

The $(AgCu)_{43}$ nanocluster underwent size disproportionation induced by a heavy Au-doping process, leading to the formation of size-reduced $(AuAgCu)_{33}$ and size-increased $(AuAgCu)_{56}$ nanoclusters. The $(AuAgCu)_{56}$ cluster molecules were crystallized in a $P2_1/c$ space group, whereas the $(AuAgCu)_{33}$ molecules were crystallized in the $P\bar{1}$ space group. The structure anatomies of $(AuAgCu)_{33}$ and $(AuAgCu)_{56}$ are illustrated in Fig. 3. The overall structure of $(AuAgCu)_{33}$ comprised an icosahedral Au_1Ag_{12} kernel that was enwrapped by two $Ag_3Cu_7(SR)_8(PPh_3)_2$ surface structures and six bridging SR ligands, making up an $Au_1Ag_{18}Cu_{14}(SR)_{14}(PPh_3)_6$ structure (Fig. 3A–D). Then, $Au_1Ag_{18}Cu_{14}(SR)_{14}(PPh_3)_6$ was stabilized by two bare sulfur ligands, likely derived from the thiol, forming the framework of the $Au_1Ag_{18}Cu_{14}S_2(SR)_{14}(PPh_3)_6$ nanocluster (Fig. 3E–G).[56,57] Besides, the structure of $(AuAgCu)_{56}$ contained a biicosahedral Au_2Ag_{21} kernel that was the same as that in $(AuAgCu)_{43}$ (Fig. 3H). Such a planar Au_2Ag_{21} kernel was capped by three $Ag_2Cu_8(SR)_8(PPh_3)_2Cl_2$ side motif structures, three $Cu_1(SR)_2(PPh_3)_1Cl_1$ surface motif structures, and two bridging Cl ligands to constitute an $Au_2Ag_{27}Cu_{27}(SR)_{30}(PPh_3)_9Cl_{11}$ structure (Fig. 3I–L). Furthermore, three bare S ligands were arranged inside the $Au_2Ag_{27}Cu_{27}(SR)_{30}(PPh_3)_9Cl_{11}$ structure, making up the final $Au_2Ag_{27}Cu_{27}S_3(SR)_{30}(PPh_3)_9Cl_{11}$ framework (Fig. 3M–O). The complete structure of $(AuAgCu)_{33}$ or $(AuAgCu)_{56}$ was triple axisymmetric with a C_3 symmetry axis passing through the center of the Au_1Ag_{12} kernel or the Au_2Ag_{21} kernel, respectively (Fig. S11†). The bond lengths between $(AuAgCu)_{33}$ and $(AuAgCu)_{56}$ nanoclusters were compared, and we found that most corresponding bonds in $(AuAgCu)_{56}$ were slightly longer than those in $(AuAgCu)_{33}$ (Fig. S12†).

The nanocluster transformation was also detectable by analyzing the optical absorption. The ultraviolet-visible (UV-vis) spectrum of $(AgCu)_{43}$ showed continuous optical absorptions with four peaks centered at 445, 537, 662, and 765 nm (Fig. 4A, blue line). After slight Au alloying, tetrametallic $(AuAgCu)_{43}$ exhibited inapparent blue-shifts relative to $(AgCu)_{43}$, and four peaks at 444, 535, 659, and 763 nm were observed (Fig. 4A, purple line). For the size disproportionation process, three absorption peaks at 421, 515, and 621 nm were observed for $(AuAgCu)_{56}$ (Fig. 4A, green line) and two UV-vis signals at 417 and 541 nm for $(AuAgCu)_{33}$ (Fig. 4A, brown line).

To further explore the size disproportionation reaction, Au doping-dependent UV-vis absorption was monitored (Fig. 4B). The absorption peaks at 445, 662, and 765 nm decreased with increasing Au doping. Additionally, the peaks at 582 nm underwent a blue shift to 537 nm, and a new absorption peak emerged at 383 nm. Besides, four isoabsorption points, centering at 375, 402, 480, and 630 nm, were observed. Such isoabsorption points demonstrated that the nanocluster transformation followed an *in situ* distortion-transformation pattern at the beginning of the Au-alloying process. In addition, since the nanocluster transformation products of the size disproportionation reaction should be a mixture, thin-layer chromatography (TLC) was exploited to separate the nanocluster mixture (Fig. S13†).[58] Two separated TLC bands were observed, and the corresponding products were determined as $(AuAgCu)_{33}$ and $(AuAgCu)_{56}$ nanoclusters by referring to the optical absorption of pure products. For the thermal stability of the obtained $(AuAgCu)_{56}$ or $(AuAgCu)_{33}$ nanoclusters, both nanoclusters were stable at 60 °C. However, the nanoclusters underwent decomposition with a further increase in temperature (Fig. S14†).

Considering that the size disproportionated $(AuAgCu)_{56}$ and $(AuAgCu)_{33}$ nanoclusters might not generate simultaneously but could convert into each other, we added $AuPPh_3Cl$ to the solution of $(AuAgCu)_{56}$ or $(AuAgCu)_{33}$ nanoclusters. $(AuAgCu)_{56}$ maintained its optical absorption with the addition of $AuPPh_3Cl$, while $(AuAgCu)_{33}$ gradually decomposed in the

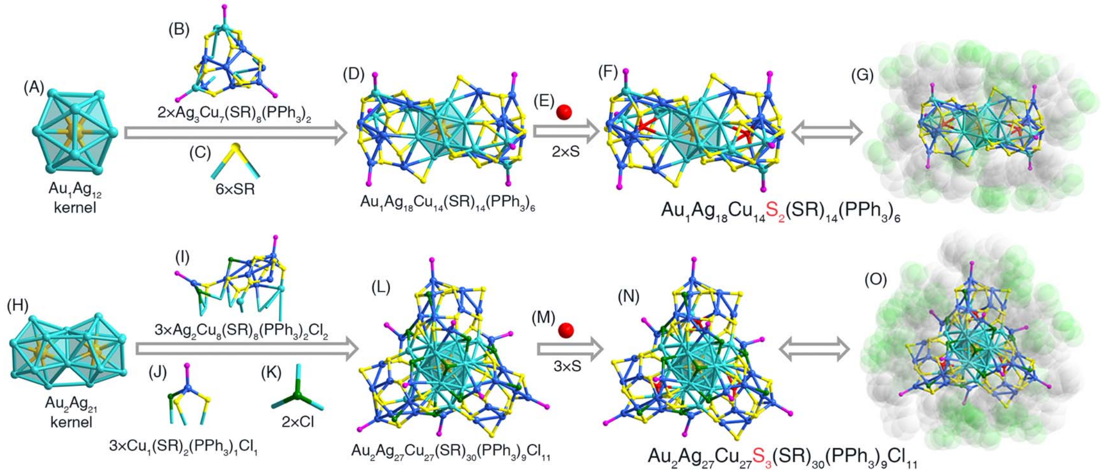

Fig. 3 Structure analyses of $(AuAgCu)_{33}$ and $(AuAgCu)_{56}$ nanoclusters. (A) Icosahedral Au_1Ag_{12} kernel. (B) Two $Ag_3Cu_7(SR)_8(PPh_3)_2$ surface structures. (C) Six bridging SR ligands. (D) The $Au_1Ag_{18}Cu_{14}(SR)_{14}(PPh_3)_6$ structure. (E) Two bare sulfur ligands. (F and G) Overall structures of the $Au_1Ag_{18}Cu_{14}S_2(SR)_{14}(PPh_3)_6$ nanocluster. (H) Biicosahedral Au_2Ag_{21} kernel. (I) Three $Ag_2Cu_8(SR)_8(PPh_3)_2Cl_2$ motif structures. (J) Three $Cu_1(SR)_2(PPh_3)_1Cl_1$ surface structures. (K) Two bridging Cl ligands. (L) The $Au_2Ag_{27}Cu_{27}(SR)_{30}(PPh_3)_9Cl_{11}$ structure. (M) Three bare sulfur ligands. (N and O) Overall structures of the $Au_2Ag_{27}Cu_{27}S_3(SR)_{30}(PPh_3)_9Cl_{11}$ nanocluster. Color labels: light blue, Ag; blue, Cu; yellow, S in thiol ligands; red, bare S ligands; magenta, P; grey, C; green, Cl. For clarity, all H atoms are omitted.

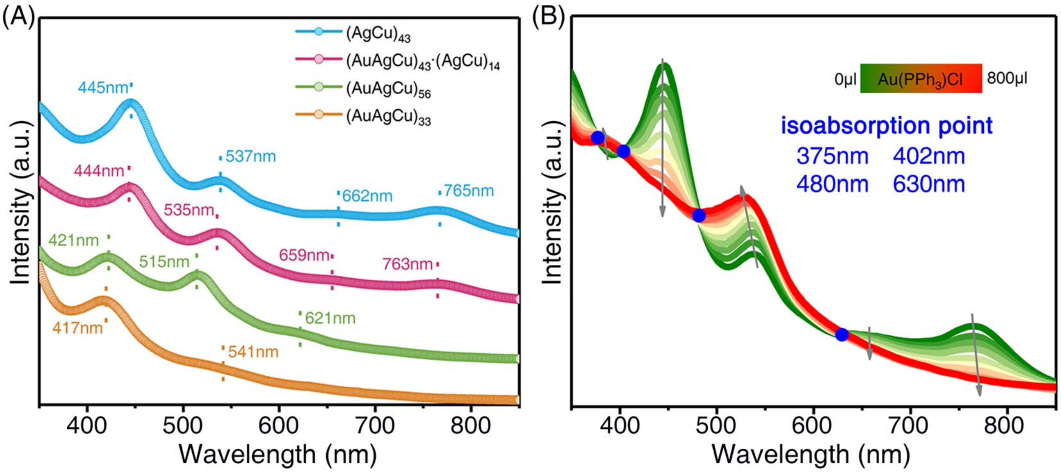

Fig. 4 Comparison of the optical absorption properties. (A) UV-vis absorption spectra of $(AgCu)_{43}$ (blue line), $(AuAgCu)_{43}\cdot(AgCu)_{14}$ (purple line), $(AuAgCu)_{56}$ (green line), and $(AuAgCu)_{33}$ (brown line) nanoclusters. (B) Au doping-dependent UV-vis absorption of the size disproportionation process.

presence of $AuPPh_3Cl$ (Fig. S15†), and no $(AuAgCu)_{56}$ was separated by TLC from these decomposition products. In this context, the $(AuAgCu)_{56}$ and $(AuAgCu)_{33}$ nanoclusters were not generated in the chronological order but were transformed from the same cluster precursor $(AuAgCu)_{43}$ at the same time, further indicating size disproportionation among the nanocluster transformations. Collectively, the transformation from $(AuAgCu)_{43}$ into $(AuAgCu)_{33}$ and $(AuAgCu)_{56}$ could be summarized as a size disproportionation reaction-$(AuAgCu)_{43}$ was transformed into a size-reduced $(AuAgCu)_{33}$ nanocluster and a size-increased $(AuAgCu)_{56}$ nanocluster in the presence of heavy Au dopants.

4 Conclusions

In summary, a bimetallic $(AgCu)_{43}$ nanocluster underwent selective size transformations under the controllable Au doping process. The slight Au alloying gave rise to a size-maintained transformation from $(AgCu)_{43}$ into $(AuAgCu)_{43}$, which was cocrystallized with $(AgCu)_{14}$ in the same crystalline unit cell. By comparison, the heavy Au alloying resulted in a size-disproportionation transformation from $(AgCu)_{43}$ into size-increased $(AuAgCu)_{56}$ and size-reduced $(AuAgCu)_{33}$. The thin layer chromatography results demonstrated the generation of $(AuAgCu)_{56}$ and $(AuAgCu)_{33}$ nanoclusters from $(AgCu)_{43}$ simultaneously, further suggesting size disproportionation among the nanocluster transformations. This work presented an important cluster platform for studying the size-maintained and size-altered transformations of metal nanoclusters, allowing for some new insights into cluster structure evolutions.

Data availability

The data that support the findings of this study are available in the ESI† of this article.

Author contributions

C. Z. and L. L. carried out experiments and analyzed the data. F. L. assisted the data analysis. X. K. and M. Z. designed the project, analyzed the data, and wrote the manuscript.

Conflicts of interest

There are no conflicts to declare.

Acknowledgements

We acknowledge the financial support of the NSFC (22371003, 22101001, and 22471001), the Ministry of Education, the University Synergy Innovation Program of Anhui Province (GXXT-2020-053), and the Scientific Research Program of Universities in Anhui Province (2022AH030009).

Notes and references

1 R. Jin, C. Zeng, M. Zhou and Y. Chen, *Chem. Rev.*, 2016, **116**, 10346–10413.
2 I. Chakraborty and T. Pradeep, *Chem. Rev.*, 2017, **117**, 8208–8271.
3 M. F. Matus and H. Häkkinen, *Nat. Rev. Mater.*, 2023, **8**, 372–389.
4 X. Kang and M. Zhu, *Chem. Soc. Rev.*, 2019, **48**, 2422–2457.
5 S. Kenzler and A. Schnepf, *Chem. Sci.*, 2021, **12**, 3116–3129.
6 E. L. Albright, T. I. Levchenko, V. K. Kulkarni, A. I. Sullivan, J. F. DeJesus, S. Malola, S. Takano, M. Nambo, K. Stamplecoskie, H. Häkkinen, T. Tsukuda and C. M. Crudden, *J. Am. Chem. Soc.*, 2024, **146**, 5759–5780.
7 K. Isozaki, K. Iseri, R. Saito, K. Ueda and M. Nakamura, *Angew. Chem., Int. Ed.*, 2024, **63**, e202312135.
8 M. Bai, L. Qin, X.-M. Z, M. Wu, L.-Y. Yao and G.-Y. Yang, *J. Am. Chem. Soc.*, 2024, **146**, 12734–12742.

9 Y. Koizumi, K. Yonesato, S. Kikkawa, S. Yamazoe, K. Yamaguchi and K. Suzuki, *J. Am. Chem. Soc.*, 2024, **146**, 14610–14619.

10 H. Yi, S. Song, S. M. Han, J. Lee, W. Kim, E. Sim and D. Lee, *Angew. Chem., Int. Ed.*, 2023, **62**, e202302591.

11 D. Arima, S. Hidaka, S. Yokomori, Y. Niihori, Y. Negishi, R. Oyaizu, T. Yoshinami, K. Kobayashi and M. Mitsui, *J. Am. Chem. Soc.*, 2024, **146**, 16630–16638.

12 L.-J. Liu, F. Alkan, S. Zhuang, D. Liu, T. Nawaz, J. Guo, X. Luo and J. He, *Nat. Commun.*, 2023, **14**, 2397.

13 Q. You, X.-L. Jiang, W. Fan, Y.-S. Cui, Y. Zhao, S. Zhuang, W. Gu, L. Liao, C.-Q. Xu, J. Li and Z. Wu, *Angew. Chem., Int. Ed.*, 2024, **63**, e202313491.

14 S. Takano, H. Hirai, T. Nakashima, T. Iwasa, T. Taketsugu and T. Tsukuda, *J. Am. Chem. Soc.*, 2021, **143**, 10560–10564.

15 J.-H. Huang, Y.-J. Liu, Y. Si, Y. Cui, X.-Y. Dong and S.-Q. Zang, *J. Am. Chem. Soc.*, 2024, **146**, 16729–16736.

16 C. A. Hosier and C. J. Ackerson, *J. Am. Chem. Soc.*, 2019, **141**, 309–314.

17 C. Zhang, W.-D. Si, Z. Wang, A. Dinesh, Z.-Y. Gao, C.-H. Tung and D. Sun, *J. Am. Chem. Soc.*, 2024, **146**, 10767–10775.

18 X. Luo, J. Kong, H. Xiao, D. Sang, K. He, M. Zhou and J. Liu, *Angew. Chem., Int. Ed.*, 2024, **63**, e202404129.

19 B. Alamer, A. Sagadevan, M. Bodiuzzaman, K. Murugesan, S. Alsharif, R.-W. Huang, A. Ghosh, M. H. Naveen, C. Dong, S. Nematulloev, J. Yin, A. Shkurenko, M. Abulikemu, X. Dong, Y. Han, M. Eddaoudi, M. Rueping and O. M. Bakr, *J. Am. Chem. Soc.*, 2024, **146**, 16295–16305.

20 Z. Liu, J. Chen, B. Li, D.-e. Jiang, L. Wang, Q. Yao and J. Xie, *J. Am. Chem. Soc.*, 2024, **146**, 11773–11781.

21 T. Kawawaki, Y. Kataoka, M. Hirata, Y. Akinaga, R. Takahata, K. Wakamatsu, Y. Fujiki, M. Kataoka, S. Kikkawa, A. S. Alotabi, S. Hossain, D. J. Osborn, T. Teranishi, G. G. Andersson, G. F. Metha, S. Yamazoe and Y. Negishi, *Angew. Chem., Int. Ed.*, 2021, **60**, 21340.

22 W.-Q. Shi, L. Zeng, R.-L. He, X.-S. Han, Z.-J. Guan, M. Zhou and Q.-M. Wang, *Science*, 2024, **383**, 326–330.

23 X. Wang, B. Yin, L. Jiang, C. Yang, Y. Liu, G. Zou, S. Chen and M. Zhu, *Science*, 2023, **381**, 784–790.

24 G. Deng, H. Yun, M. S. Bootharaju, F. Sun, K. Lee, X. Liu, S. Yoo, Q. Tang, Y. J. Hwang and T. Hyeon, *J. Am. Chem. Soc.*, 2023, **145**, 27407–27414.

25 Q. Liu, X.-Y. Zhai, R.-J. Jian and L. Zhao, *Chem. Sci.*, 2024, **15**, 11311–11320.

26 X. Wei, H. Li, H. Li, Z. Zuo, F. Song, X. Kang and M. Zhu, *J. Am. Chem. Soc.*, 2023, **145**, 13750–13757.

27 X. Wei, K. Chu, J. R. Adsetts, H. Li, X. Kang, Z. Ding and M. Zhu, *J. Am. Chem. Soc.*, 2022, **144**, 20421–20433.

28 R. Saito, K. Isozaki, Y. Mizuhata and M. Nakamura, *J. Am. Chem. Soc.*, 2024, **146**, 20930–20936.

29 C. Zhang, W.-D. Si, Z. Wang, C.-H. Tung and D. Sun, *Angew. Chem., Int. Ed.*, 2024, **63**, e202404545.

30 F. Sun, L. Qin, Z. Tang, G. Deng, M. S. Bootharaju, Z. Wei, Q. Tang and T. Hyeon, *Chem. Sci.*, 2023, **14**, 10532–10546.

31 Z. Wang, R. K. Gupta, F. Alkan, B.-L. Han, L. Feng, X.-Q. Huang, Z.-Y. Gao, C.-H. Tung and D. Sun, *J. Am. Chem. Soc.*, 2023, **145**, 19523–19532.

32 X. Kang, L. Huang, W. Liu, L. Xiong, Y. Pei, Z. Sun, S. Wang, S. Wei and M. Zhu, *Chem. Sci.*, 2019, **10**, 8685–8693.

33 P. Chandrashekar, G. Sardar, T. Sengupta, A. C. Reber, P. K. Mondal, D. Kabra, S. N. Khanna, P. Deria and S. Mandal, *Angew. Chem., Int. Ed.*, 2024, **63**, e202317345.

34 Y. Saito, A. Suda, M. Sakai, S. Nakajima, Y. Shichibu, H. Kanai, Y. Ishida and K. Konishi, *Chem. Sci.*, 2024, **15**, 11775–11782.

35 J. Liu, Y. Sato, V. K. Kulkarni, A. I. Sullivan, W. Zhang, C. M. Crudden and J. E. Hein, *Chem. Sci.*, 2023, **14**, 10500–10507.

36 S. Gratious, S. Mukherjee and S. Mandal, *J. Phys. Chem. Lett.*, 2022, **13**, 9014–9027.

37 T.-A. D. Nguyen, Z. R. Jones, D. F. Leto, G. Wu, S. L. Scott and T. W. Hayton, *Chem. Mater.*, 2016, **28**, 8385–8390.

38 K. Yonesato, S. Yamazoe, S. Kikkawa, D. Yokogawa, K. Yamaguchi and K. Suzuki, *Chem. Sci.*, 2022, **13**, 5557–5561.

39 A. Jana, M. Jash, A. K. Poonia, G. Paramasivam, M. R. Islam, P. Chakraborty, S. Antharjanam, J. Machacek, S. Ghosh, K. N. V. D. Adarsh, T. Base and T. Pradeep, *ACS Nano*, 2021, **15**, 15781–15793.

40 J. A. Kephart, C. G. Romero, C.-C. Tseng, K. J. Anderton, M. Yankowitz, W. Kaminsky and A. Velian, *Chem. Sci.*, 2020, **11**, 10744–10751.

41 L.-L. Yan, L.-Y. Yao, M.-Y. Leung and V. W.-W. Yam, *CCS Chem.*, 2021, **3**, 326–337.

42 L. Yang, X.-Y. Wang, X.-Y. Tang, M.-Y. Wang, C.-Y. Ni, H. Yu, Y.-L. Song, B. F. Abrahams and J.-P. Lang, *Sci. China: Chem.*, 2022, **65**, 1094–1099.

43 Z. Wang, H.-F. Su, C.-H. Tung, D. Sun and L.-S. Zheng, *Nat. Commun.*, 2018, **9**, 4407.

44 Z. Wang, Y.-J. Zhu, Y.-Z. Li, G.-L. Zhuang, K.-P. Song, Z.-Y. Gao, J.-M. Dou, M. Kurmoo, C.-H. Tung and D. Sun, *Nat. Commun.*, 2022, **13**, 1802.

45 Z. Wang, J.-W. Liu, H.-F. Su, Q.-Q. Zhao, Mo. Kurmoo, X.-P. Wang, C.-H. Tung, D. Sun and L.-S. Zheng, *J. Am. Chem. Soc.*, 2019, **141**, 17884–17890.

46 Y. Li, H. K. Kim, R. D. McGillicuddy, S.-L. Zheng, K. J. Anderton, G. J. Stec, J. Lee, D. Cui and J. A. Mason, *J. Am. Chem. Soc.*, 2023, **145**, 9304–9312.

47 T. Ree, *J. Chem. Educ.*, 1971, **48**, 467.

48 S. Zhu, L. Yang, Y. Long, M. Gao, T. Huang, W. Hang and X. Yan, *J. Am. Chem. Soc.*, 2010, **132**, 12176–12178.

49 A. Letzel, B. Gökce, A. Menzel, A. Plech and S. Barcikowski, *Appl. Surf. Sci.*, 2018, **435**, 743–751.

50 L. G. AbdulHalim, M. S. Bootharaju, Q. Tang, S. Del Gobbo, R. G. AbdulHalim, M. Eddaoudi, D.-e. Jiang and O. M. Bakr, *J. Am. Chem. Soc.*, 2015, **137**, 11970–11975.

51 X. Kang, S. Wang and M. Zhu, *Chem. Sci.*, 2018, **9**, 3062–3068.

52 Y. Niihori, N. Takahashi and M. Mitsui, *J. Phys. Chem. C*, 2020, **124**, 5880–5886.

53 X. Kang, Y. Li, M. Zhu and R. Jin, *Chem. Soc. Rev.*, 2020, **49**, 6443–6514.

54 S. Jin, X. Zou, L. Xiong, W. Du, S. Wang, Y. Pei and M. Zhu, *Angew. Chem., Int. Ed.*, 2018, **57**, 16768.

55 X. Zou, S. He, X. Kang, S. Chen, H. Yu, S. Jin, D. Astruc and M. Zhu, *Chem. Sci.*, 2021, **12**, 3660–3667.

56 D. Crasto, S. Malola, G. Brosofsky, A. Dass and H. Häkkinen, *J. Am. Chem. Soc.*, 2014, **136**, 5000–5005.

57 X. Wei, C. Xu, H. Li, X. Kang and M. Zhu, *Chem. Sci.*, 2022, **13**, 5531–5538.

58 A. Ghosh, J. Hassinen, P. Pulkkinen, H. Tenhu, R. H. A. Ras and T. Pradeep, *Anal. Chem.*, 2014, **86**, 12185–12190.